Dynamics and control of internal transport barriers in reversed shear discharges

D. E. Newman, B. A. Carreras, and D. Lopez-Bruna
Oak Ridge National Laboratory, Oak Ridge, Tennessee 37831-8071

P. H. Diamond and V. B. Lebedev
University of California at San Diego, La Jolla, California 92093-0319

Transitions to an enhanced confinement regime in tokamak plasmas with negative central magnetic shear have been observed in a number of devices. A simple model incorporating the nonlinear coupling between the turbulent fluctuations and the sheared radial electric field is added to a transport model in order to investigate the dynamics of the transition to this enhanced confinement mode. In this model, by incorporating both the instability growth rate profiles and particle and/or power deposition profiles, a rich variety of transition dynamics is uncovered. Transition dynamics and their concomitant thresholds are examined within the context of these models. In the course of investigating these transitions, potential methods for triggering and controlling these enhanced confinement regimes have been discovered and are discussed. © *1998 American Institute of Physics.* [S1070-664X(98)02904-8]

I. INTRODUCTION

The first internal transport barriers in magnetically confined plasmas were observed in the Japan Tokamak-60 (JT-60),[1] Princeton Beta Experiment-Modification (PBX-M),[2] and Alcator C tokamaks.[3] This type of transport barrier, in contrast to the high-confinement mode (H-mode)[4] barrier, is formed independently of the edge plasma conditions. Therefore, these barriers are more amenable to understanding the basis of the plasma dynamics. Recently, detailed investigation of plasma discharges in which modification of the current profile leads to a region in the core with weak or negative magnetic shear has caused a great deal of excitement. The reason for this interest is the observation that not only do these weak central shear (WS) or negative central shear (NCS), discharges exhibit improved confinement, but they also allow access to a regime of further enhancement through formation of an internal transport barrier following a bifurcation.[5–8] This enhanced reversed shear (ERS) regime is accessed through a confinement bifurcation in which the most direct but not unique control parameter is the power deposited inside the radius at which the magnetic shear is reversed. The transition to enhanced confinement is characterized by a total or near total suppression of the anomalous particle and ion heat transport and a possible reduction in the levels of neoclassical transport due to strong E_r effects. One of the practical difficulties with operation in such regimes is that confinement is so good it leads to a large accumulation of the particles and heat deposited within the enhanced confinement region. For steady-state operation, this leads to challenges in controlling the confinement to prevent impurity accumulation, particle overload, or macroscopic instability. If the ERS regime can be reproducibly triggered (at reasonable powers) and controlled (in a reactor relevant environment), this regime then offers a metaphorical bridge over the bubbling caldron which is anomalous transport. The meta-

phorical mechanism is via the sheared $E \times B$ flow parting the bubbling waters of the reddish-hued plasma sea.

The general philosophy behind the models presented here is that rather than initially building a comprehensive model with all possible physical effects, we first assemble a finite set of dynamical components into a hierarchy of simple models to investigate the importance of those individual pieces. Then we build a more complete model to gain quantitative insight into the dynamics of the transition when coupled to a realistic transport model. The heuristics of the underlying model[9,10] are simple and general (Fig. 1). The necessary pieces are as follows. First, a radially dependent profile of the turbulent instability growth rates, $\gamma(r)$, is essential. This dependence comes predominantly from the radial profile of q. Where the magnetic shear is weak or reversed (negative), many instability growth rates are greatly reduced,[11–13] leading to a gradient in the γ profiles. Other mechanisms that can affect the local growth rates and growth rate profiles are the dynamic Shafranov shift feedback on γ,[14] and the effect of shear in the diamagnetic frequency on γ. Growth rate profiles of the micro-instabilities calculated from experimental profiles exhibit such a gradient[15] around the shear reversal point. The other necessary element is the coupling of the temperature, density, and flow velocity profiles to fluctuation intensity levels through the radial electric field shear. The basic model is then simply the nonlinear coupling of the radial profile evolution via the radial electric field to the turbulence. As the power (or particles) deposited increases, the profiles steepen, leading to increased turbulent fluctuations (through the gradient drive) but also to an increase in the radial electric field (also through the modified gradient). Because the suppression of the turbulence is dependent on the square of the gradient in the electric field, a critical power can exist below which increasing power increases the turbulence (and therefore, the turbulent diffusion)
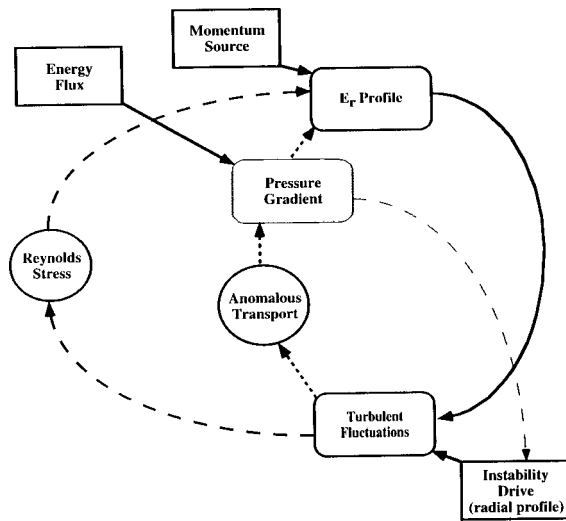
FIG. 1. Schematic picture of the feedback loops that enable a transition to enhanced confinement.

while above which the sheared radial electric field dominates and the turbulent fluctuations (and diffusion) are suppressed. In this regime, the residual transport is predominantly collisional.

The generic concepts of this transition model have been described in Ref. 10. Here, we concentrate on examining a more detailed description of the dynamics of the transition, including the coupling to a transport model that independently evolves the ion and electron temperatures, density, and toroidal velocity profiles. By using the transport model, it is possible to quantitatively evaluate the power threshold and to study its scaling with plasma parameters. A basic scaling model of the threshold is presented and compared to the results of transport simulations. By better understanding the mechanisms of the transition, it is possible to suggest methods for controlling the internal transport barriers. In Table I, the main profile parameters and their controls are identified and possible control techniques are listed. Control is important for two reasons: (1) improved control facilitates access to these high-confinement regimes, and (2) it could be important to periodically lower the barrier to facilitate control of particle and impurity accumulation, stability, etc., while still maintaining the overall enhanced confinement.

The remainder of the paper is organized as follows. Section II contains a description of the transition dynamics based on a two-field model for the E_r'-driven internal transport barriers. The effect of toroidal velocity shear on the transition is described in Sec. III. Section IV then contains a more comprehensive version of this model including the

coupling to ion temperature, electron temperature, and density. This model is used to evaluate the power threshold and its scaling. This is followed by some examples of triggering mechanisms and possible control schemes in Sec. V. Section VI contains the conclusions.

II. TRANSITION DYNAMICS IN A TWO-FIELD MODEL

To investigate the core transport bifurcation mechanisms associated with the formation of internal transport barriers, we begin with a model for the fluctuation intensity and profile dynamics that generalizes the local transition models investigated earlier.[16–19] This model contains a system of equations with the necessary physics to capture the basic transition dynamics. The simplest form of such a model is the following two-field system:

$$\frac{\partial \varepsilon}{\partial t} = [\gamma_0(r)N - \alpha_1 \varepsilon - \alpha_2 \langle V_E \rangle'^2] \varepsilon + \frac{\partial}{\partial r} \left(D_\varepsilon \frac{\partial \varepsilon}{\partial r} \right), \quad (1)$$

$$\frac{\partial N}{\partial t} = S(r) + \frac{\partial}{\partial r} \left[(D_{1N} + D_{2N}\varepsilon) \frac{\partial N}{\partial r} \right]. \quad (2)$$

In this model ε is the local fluctuation intensity defined as $\varepsilon = \langle (\tilde{n}/n)^2 \rangle^{1/2}$ and N is the normalized pressure gradient defined as $N \equiv (a/\langle P_i \rangle)(-d\langle P_i \rangle/dr)$, where a is the plasma minor radius and P_i is the ion pressure. The angular brackets, $\langle \rangle$, indicate flux surface averaging. For the present calculations, the density gradient (dn/dr) is taken to be the dominant component of the pressure gradient. This assumption will be relaxed in Sec. IV where the model is expanded to include separate evolution of density and temperature.

In the fluctuation equation, $\gamma_0(r)N$, which is written in separable form, corresponds to the linear growth rate of the pressure-gradient-driven microinstability underlying the turbulence in the absence of electric field shear. Here, $\gamma_0(r)$ is a geometrical factor in the growth rate that describes the magnetic shear stabilization effect as a function of radius. For the reversed magnetic shear discharges, we assume that the safety factor q profile has a minimum at the radial position r_{min}, $q_{min} = q(r_{min})$, and the reversed shear region is for $r < r_{min}$. Because of the shear stabilization effect, $\gamma_0(r)$ is reduced, but different from zero, for $r < r_{min}$. The radial dependence of the source, q, and γ_0 profiles used in these calculations is shown in Fig. 2.

The parameters α_1 and α_2 are dependent on the particular instability dynamics of the transport model. However, it is possible to derive a "generic" scaling form for these coefficients. The parameter α_1 is determined by the saturation level of the instability in the low-confinement regime and

TABLE I. Mechanism for profile modification.

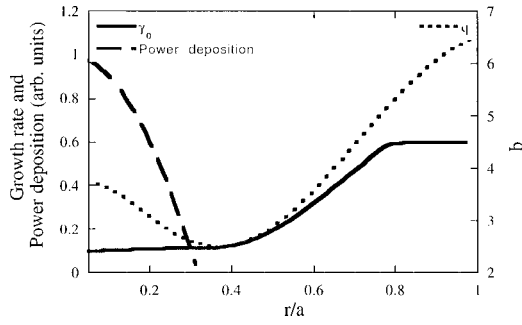| Profile parameter	Control parameter	Control technique
L_n	Particle flux Γ	Pellet injection
L_{T_i}	Heat flux Q_T	Modulated NBI heat pulse[a]
L_{V_ϕ}	Momentum torque τ_ϕ	NBI/IBW
q'	Toroidal current J	Current drive

[a]NBI=neutron beam injection.

FIG. 2. Radial profiles of γ_0 (solid line), power deposition (long dash), and q (short dash).

scales as $\alpha_1 \propto (\sqrt{\overline{k_\theta^2}}\rho_s c_s / W_k)$. The other parameter, α_2, is determined from the $E \times B$ shear flow suppression criterion,[20] and it scales as $\alpha_2 \propto (\overline{k_\theta^2} W_k^2 / \overline{\gamma_0})$. In these expressions, $c_s = \sqrt{T_e/m_i}$ is the speed of sound, $\rho_s = c_s/\Omega_i$ is the sound Larmor radius, k_θ is the poloidal wave number, and W_k is the radial width of the instability. Here, the bar on k_θ indicates spectral average. In Eq. (2), $S(r)$ is the radial derivative of the source term and the diffusivity, $D_n \equiv D_{1N} + D_{2N}\varepsilon$, has two components. The first corresponds to neoclassical transport, $D_{\mathrm{neo}} \equiv D_{1N}$, and the second, $D_{\mathrm{anom}} \equiv D_{2N}\varepsilon$, is because of turbulent transport. For this model, all coefficients, D_{iN} and D_ε, are taken to be constant in time and space.

The system of equations is closed by the radial ion force balance equation

$$\langle V_E \rangle \equiv -\frac{E_r}{B} = \langle V_\theta \rangle - \frac{B_\theta}{B}\langle V_\varphi \rangle - \frac{1}{eB_z n}\frac{dP_i}{dr}. \tag{3}$$

From this equation, one can calculate the sheared $E \times B$ flow term in the fluctuation equation

$$\langle V_E \rangle' = \langle V_\theta \rangle' - \frac{B_\theta}{B}\langle V_\varphi \rangle' - \alpha N^2, \tag{4}$$

where the primes indicate radial derivative and $\alpha \equiv \rho_i V_i/a^2$. Here, V_i is the ion thermal velocity. In deriving Eq. (4), we have neglected the radial derivative of the poloidal field and the second derivative of the profiles. Because the magnetic pumping in the core is thought to be large enough to effectively damp out any poloidal flow, we will take V_θ to be zero. This, of course, need not always be true, because of possible viscosity breakdown for the high electric fields which occur in ERS plasmas. There is, in fact, some evidence that a localized spike in poloidal flow may trigger some ERS transitions in the Tokamak Fusion Test Reactor (TFTR).[21] It should also be noted that this damping is on the physical poloidal flow alone and not on the diamagnetic component of the $E \times B$ flow. We initially also set the toroidal flow V_ϕ to zero for simplicity in understanding the transition. Because the poloidal sheared flow is taken to be damped, and initially the toroidal sheared flow is set to zero, the dominant, or even the only, contribution to the radial electric field [V_E in Eq. (3)] is the diamagnetic term. However, because some (though not all) of the magnetic confinement devices that observe this transition also have large

shear in the toroidal flow coincident with the barrier position, we investigate the effect of the evolution of the toroidal flow in the next section.

This system of equations is nearly the same as the one used in studying the propagation of confinement improvement fronts from the plasma edge in the study of the very-high-confinement mode (VH mode).[22] However, two important differences exist: (1) the radial dependence of the linear growth rate that carries the information on the magnetic shear stabilization and (2) the radial dependence of the source profile. This new information is critical for understanding the reversed magnetic shear configuration's enhanced confinement regimes.

Stationary solutions of this model are calculated by setting the time derivatives to zero in Eqs. (1) and (2). Neglecting the diffusion term in the fluctuation equation, the stationary states are the solution of the following equation:

$$\Gamma(r, N, N') \equiv D_{1N}\frac{\partial N}{\partial r} + \frac{D_{2N}}{\alpha_1}(\gamma_0 - \alpha_2\alpha^2 N^3)N\frac{\partial N}{\partial r} = S_I(r), \tag{5}$$

where Γ is the gradient of the particle flux and $S_I(r)$ is the integrated source term,

$$S_I(r) \equiv \int_0^r S(r')dr'. \tag{6}$$

From a local perspective, two types of solutions depend on the sheared electric field strength. In the prelude phase, the sheared electric field is weak, and confinement is dominated by anomalous transport. In this phase, the fluctuation level is high, $\varepsilon = \gamma_0(r)N/\alpha_1$, and so is the anomalous diffusivity. It should be noted, however, that the core fluctuation level and, therefore, the core transport is reduced from the standard low-confinement mode (L mode) by the reduction of the linear growth rates in the core because of the reversed magnetic shear; that is, $\gamma_0(r)$ is small for $r < r_{\min}$. The density profile is given by

$$\frac{\partial N^2}{\partial r} = 2\frac{\alpha_1 S_I(r)}{\gamma_0(r)D_{2N}}. \tag{7}$$

The second solution is the posttransition equilibrium. This solution is characterized by steep gradients up to the final barrier position because of the complete suppression of the turbulent transport inside the barrier region ($\varepsilon = 0$). No assumption about marginal stability is made as the marginally stable profile self-consistently changes in the presence of a sheared radial electric field. For this solution, the density gradient is

$$\frac{\partial N}{\partial r} = \frac{S_I(r)}{D_{1N}}. \tag{8}$$

Equations (7) and (8) give the local solutions, but we are interested in the global structure of profiles predicted by this model. The pretransition state corresponds to the integrated profile given by Eq. (7). However, after the transition, the solution is a combination of a solution of the type given by Eq. (8) in the inner part of the plasma that must be matched to the outer solution given by Eq. (7). In Ref. 10, we consid-

Phys. Plasmas, Vol. 5, No. 4, April 1998

Newman *et al.* 941

ered a simpler model in which the flux is only a function of r and N. For this simpler model, it was possible to graphically understand the feasibility of a matching solution (existence of a transport barrier) through the topography of the flux landscape.[10] Here, because of the increased complexity, it is much more difficult to visualize the matching.

As described earlier, the basic feedback mechanism responsible for the transition is quite simple. When the power deposited inside the q_{min} surface causes the local flux through the q_{min} surface to create a pressure gradient such that E_r' exceeds the value needed to suppress the local turbulence, the turbulence level falls, the gradient further steepens, and a positive feedback loop is created. The transition will typically initiate right outside the q_{min} surface where the gradient flattens again, because of the increase in the fluctuations. Locally the transition criterion is

$$S_{crit} = \frac{\gamma_0 D_{2N}}{2\alpha_1} \frac{\partial}{\partial r} \left[\left(\frac{\gamma_0}{\alpha_2 \alpha^2} \right)^{2/3} \right]. \tag{9}$$

Equation (9) can be thought of as defining a critical flux through the local surface. This critical flux, which in steady state is equivalent to the rate of particle or energy deposition inside the surface, is proportional to the local linear growth rate of the instability. It is, therefore, clear that the deposition profiles of the power, particles, and momentum (as we will show later) relative to the radial profiles of the growth rate are of critical importance and, in fact, can move the location at which the transition initiates. It should also be noted that there are many routes to the bifurcation point. The power is the most obvious; however, changing the growth rates (or the growth rate profiles) can have the same effect as the system locally undergoes a transition at a critical value of γ. A method for giving insight into the multiple bifurcation routes and the symmetry of those routes can be gained via the flux landscape picture.

Because of the positive feedback in this type of transition, once the transition is initiated at a given radial point, it effectively ''bootstraps'' itself both in and out, covering the entire region that is supercritical and the region that is critical at the posttransition diffusivity (the neoclassical or adjusted neoclassical level). Supercritical means that in steady state, with the pretransition fluctuation levels, the local threshold is exceeded. Even though in steady state the threshold may be exceeded in much of, or even the entire, reversed shear region, the transition cannot happen simultaneously in all radial positions. The reason is that the flux is temporarily reduced outside the transitioned region. This reduction in the flux locally suppresses the transition in the nearby region and leads to the progressive dynamics of the transition [see Figs. 3(a) and 3(b)]. Figure 3(a) shows profiles of the fluctuation level at various times after the critical power has been exceeded. The transition generally initiates at the radial location where the growth rate starts to increase, the q_{min} surface, which is also the location in this model that has the largest flux (in the reduced growth rate region). Therefore E_r' has a maximum at r_{min}. The transition starts where the gradients change the most, making E_r' locally the largest. This is generally caused by the confinement im-
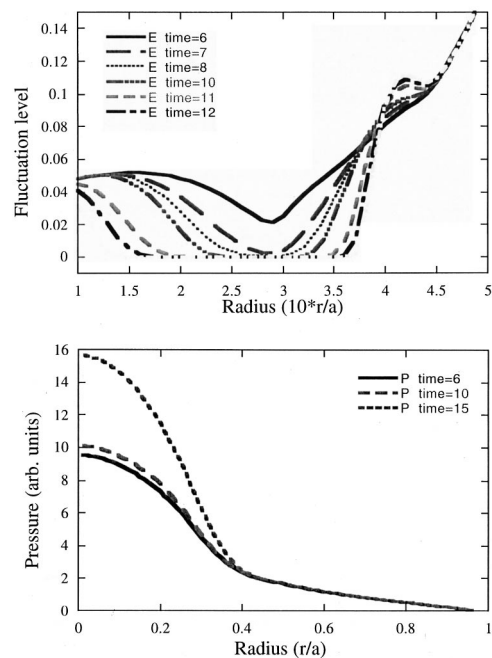

FIG. 3. Profiles of the fluctuation level (E) [panel (a)] and pressure [Panel (b)] at a sequence of times during a transition. Note the transition propagates both inward and outward from the point of initiation ($r/a \sim 0.3$), as seen in E.

provement because of the reversed shear region and is therefore localized near the q_{min} surface. In a more comprehensive model, important modifications to the initiation point can come from both the q profile and the deposition profile. These effects are discussed in Sec. IV.

The transition propagates outward until it can no longer bootstrap itself up the growth rate beach, and inward all the way. Figure 3(b) shows three pressure profiles after the transition. Because the only residual transport is neoclassical, the pressure profiles grow and move outward. In the core region, the transition propagates from its initiation point inward and outward as a front, that is, with a nearly self-similar transition profile [see Fig. 3(a)]. When this transition front reaches the region of increasing γ_0, the distance of penetration is dependent on two factors: first, the power deposited inside the q_{min} surface and, second, the breadth of the region of increasing γ_0. Figure 4(a) shows two before-and-after fluctuation level profiles, one for a broad γ_0 profile and one for a narrower one [Fig. 4(b)]. The final (edge) level of γ_0 is the same for these two cases; only the width (W) of the region connecting the low growth rate (reversed shear region) to the edge region is changed. Figure 4(a) illustrates that the barrier end point or foot propagates further out in the case of the broad transition region. This is similar (but not exactly isomorphic) to a tide moving up a beach: a more gently sloping beach allows the tide to move much further inland than a steep beach. The power dependence of the final barrier foot point is illustrated by Fig. 5, which shows that the barrier moves out as the power increases above the critical power. To estimate the position of the barrier footprint using the model of Ref. 23, we have to determine the Maxwell flux,
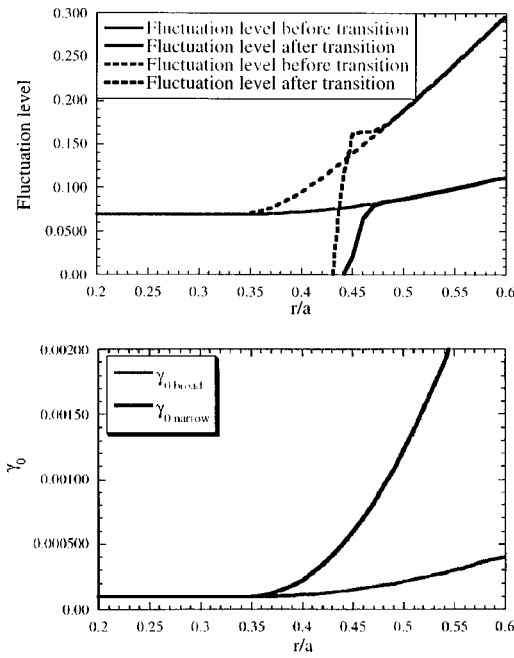
FIG. 4. Steady-state profiles of the fluctuation level before and after transition [panel (a)] for 2 γ_0 profiles [panel (b)]. Solid (dashed) lines in panel (a) represent the broad (narrow) γ_0 profile.

which is less than the critical flux for suppression, for the present model. For $D_{1N} \ll D_{2N}$, we have

$$\Gamma_M \approx \gamma_0(r)^{2/3} \sqrt{\frac{D_{1N} D_{2N}}{3 \alpha_1 (\alpha^2 \alpha_2)^{1/2} L^2}}, \tag{10}$$

where L is a typical scale length for the density profile. Because we have used the following form for the radial dependence of the linear growth rate in the numerical calculation, $\gamma_0(r) = \gamma_{01} + \gamma_{02} \tanh[(r - r_{\min})/W]$, the footprint position should vary with the input power (P) as

$$\frac{r}{a} = \frac{r_0}{a} + \frac{W}{a} \ln \left[\frac{(P/P_{\text{crit}})^{3/2} - 1}{A - (P/P_{\text{crit}})^{3/2}} \right]. \tag{11}$$

Equation (11) describes well the results of the numerical calculation as shown in Fig. 5.

One of the more important features of this system is the hysteresis in power at the transition. This large difference in threshold power (P_{crit}) between the forward transition and
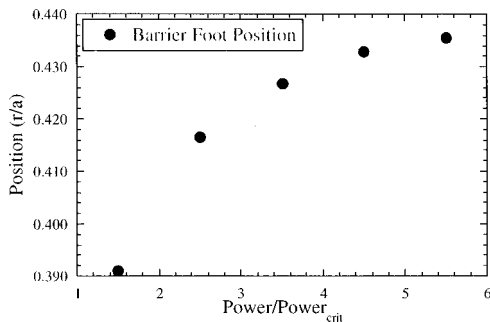

FIG. 5. The radial position of the end point of the enhanced confinement region (the barrier foot point) as a function of the power input normalized to the critical power.
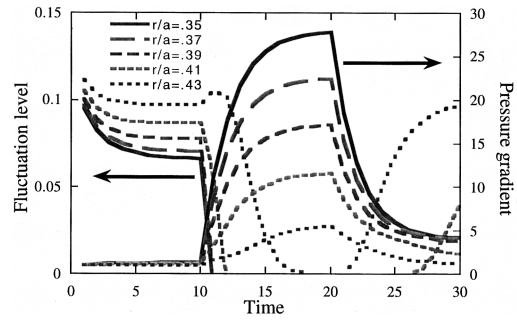

FIG. 6. Time histories of the fluctuation level and pressure gradient at five radial positions. The power is stepped up at $t = 10$, causing a transition, and stepped back down at $t = 20$. The back transition does not occur due to the hysteresis in the system.

the backward transition has been observed experimentally[24] and can be readily understood in terms of the model presented here. The hysteresis can be a very valuable feature because it can take many times less power to hold the system in the enhanced confinement mode than it does to initially get into that state. This large power difference suggests some interesting methods for triggering and controlling the ERS regime, which will be explored later. To study this effect in the present model, we use as a control parameter the value of the integrated source, $P \equiv S_1(a)$, as an effective power. Even in this most minimal version of the transition model the hysteresis effect is shown (Fig. 6). At normalized time $t = 10$, the ''power'' is increased from $P = 0.5 P_{\text{crit}}$ to $P = 2.0 P_{\text{crit}}$. The time traces of the fluctuation level and pressure gradient at different radial locations show the transition moving outward. The fluctuations are sequentially quenched and the pressure gradients rise dramatically. At $t = 20$, the effective power is turned back down to the original pretransition level; however, the back transition only occurs at the two farthest out radii. This change is shown in both the fluctuation level traces, which do not rise again, and in the pressure gradient traces that have fallen (because the source is decreased) but are still about five times their pretransition level. This asymmetry can be readily understood from the realization that the true control parameter in this system is really the local pressure gradient N, which determines the local E_r. Because in steady state the energy (particle) flux Γ_n through a surface is simply equal to the power (particles) deposited inside that surface, with a given diffusivity ($D_n = \Gamma_n / \nabla n$), we can see that to maintain a gradient, $\nabla n_{\text{crit}} = \Gamma_n / D_n$, at the pretransition value with a pretransition diffusivity (which includes the anomalous diffusion) a large flux (and therefore large source) is required. However, after the transition, the diffusivity is neoclassical and therefore the needed flux (''power'') is greatly reduced. From this argument, we see that $P_{\text{crit}\uparrow} / P_{\text{crit}\downarrow}$ is related to $D_{\text{anom}} / D_{\text{neo}}$. Here, $P_{\text{crit}\uparrow}$ ($P_{\text{crit}\downarrow}$) is the critical power for the forward (backward) transition. Using the transition model of Ref. 10, which is a variant of the model considered here but which is amenable to analysis, we obtained

$$\frac{P_{\text{crit}\uparrow}}{P_{\text{crit}\downarrow}} = \frac{1}{\sqrt{3}} \left(\frac{D_{\text{anom}}}{D_{\text{neo}}} \right)^{3/4}. \tag{12}$$
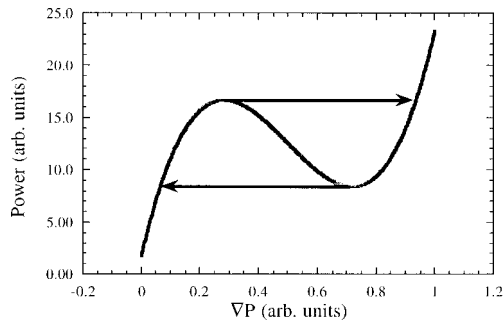
FIG. 7. A schematic representation of the hysteresis curve in power versus pressure gradient space. This plot highlights the different powers at which the forward and backward transitions occur.
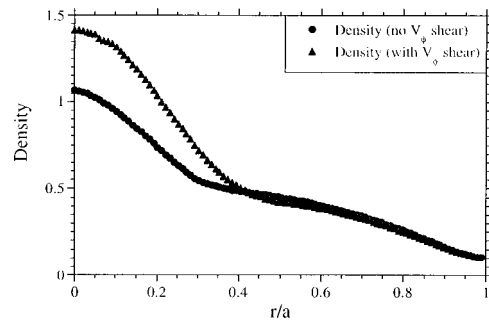

FIG. 8. The density profile is shown for two cases, one with sheared toroidal flow (solid triangle) and one without sheared toroidal flow (solid dot), both at 12 MW and with all other parameters the same. The case with the sheared flow added has transitioned and is still evolving on axis.

This hysteresis cycle can also be visualized in the standard way via an S-shaped bifurcation curve, with the forward transition occurring at the high ''power'' top of the S-curve and the back transition occurring at the much lower ''power'' bottom of the S-curve (see Fig. 7 for example).

III. EFFECT OF THE TOROIDAL VELOCITY SHEAR ON THE TRANSITION DYNAMICS

To help in accessing the enhanced confinement regime one can look at the equation for the radial electric field [Eq. (3)] and observe that the two pieces we have ignored until now, V_ϕ and V_θ, can play important roles. Because there is no damping of V_ϕ (as there is in the case of V_θ) in the core the sheared toroidal flow, V'_ϕ, can have an effect comparable to or even exceeding the ∇P_i component. This sheared toroidal flow can come from unbalanced beams or even beams that are simply radially unbalanced (i.e., the coinjected beam may deposit power and particles at a different radius than the counterinjected beam). The effect of this V'_ϕ can be to reduce the ''power'' (or net particle flux) threshold by reducing the amount of E'_r that needs to be contributed by the pressure gradient. It should be noted that the sign of the V'_ϕ term can either add to or subtract from the ∇P_i term, which means that the threshold can actually be moved up or down which again is interesting in terms of control, particularly when operating near the back transition threshold. Within the confines of our minimal model, this effect can be looked at by adding an evolution equation for $\langle V'_\phi \rangle$:

$$\frac{\partial \langle V'_\phi \rangle}{\partial t} = \alpha_7 \langle V'_E \rangle \varepsilon + \tau_\phi + \frac{\partial}{\partial r}\left[(D_{1\phi} + D_{2\phi}\varepsilon)\,\frac{\partial \langle V'_\phi \rangle}{\partial r}\right]$$
$$- \mu \langle V'_\phi \rangle. \tag{13}$$

Here μ is the damping because of collisions or magnetic braking, which is usually feeble compared to the poloidal flow damping rate; α_7 is the coefficient of the Reynolds stress drive (which is generally very small for the toroidal flow), and τ_ϕ is the sheared torque (i.e., because of the beams, momentum deposition profile). The third term on the right is the anomalous toroidal momentum diffusion term, which we assume has the same form as the anomalous particle transport. We also assume that the Reynolds stress term is very small relative to τ_ϕ and find that, depending on the sign of τ_ϕ, we can cause transitions at lower powers or

inhibit them. In Fig. 8 the central density is shown for a case without V'_ϕ with a subcritical power, and a case with V'_ϕ and the same power. The transition to the enhanced confinement can be seen in the latter case as the central density bifurcates when V'_ϕ is turned on and the system transitions into an enhanced confinement regime.

Similar arguments can be made for the poloidal flow. However, V_θ cannot adjust itself unless an external drive exists because of the strong damping from magnetic pumping. Nevertheless, if a local flow can be created via some external mechanism[25] [Ion Bernstein Wave (IBW) drive,[26] for example], one could locally reduce the power threshold, allowing easier access to the ERS regime, with the added benefit that once in the ERS state, the needed power goes down dramatically because of hysteresis.

IV. TRANSITION DYNAMICS WITH FULL TRANSPORT MODEL AND EVALUATION OF THE POWER THRESHOLD

While the transition dynamics and threshold effects from the minimal model are interesting and suggest a qualitative description of the mechanisms for the formation and control of internal barriers, a reasonable case can be made that, in a more complete transport model (i.e., one that evolves ion temperature, T_i, electron temperature, T_e, and density, n, in addition to the fluctuation level), the transition thresholds and transition dynamics may be different. Importantly, this type of model also allows the parameters in the fluctuation equation to evolve on the appropriate transport time scale and includes the radial dependence of those parameters on the transport quantities. To investigate this possibility and to calculate the power threshold for meaningful experimental parameters, such a model is used. The model is essentially the result of coupling a one-dimensional transport model to the fluctuation evolution equation:

$$\frac{\partial n}{\partial t} = S_{NBI} + S_{gp} + \frac{1}{r}\frac{\partial}{\partial r}\left[r D_n \frac{\partial n}{\partial r}\right], \tag{14}$$

$$\frac{3}{2}\frac{\partial n T_i}{\partial t} = \frac{1}{r}\frac{\partial}{\partial r}\left[r\left(\chi_i n \frac{\partial T_i}{\partial r} + \frac{5}{2} D_n T_i \frac{\partial n}{\partial r}\right)\right] - D_n \frac{1}{n}\frac{\partial n}{\partial r}\frac{\partial n T_i}{\partial r}$$
$$+ Q^i_{NBI} + Q_{ei}(T_e - T_i), \tag{15}$$

$$\frac{3}{2}\frac{\partial nT_e}{\partial t} = \frac{1}{r}\frac{\partial}{\partial r}\left[r\left(\chi_e n\,\frac{\partial T_e}{\partial r}+\frac{5}{2}\,D_n T_e\,\frac{\partial n}{\partial r}\right)\right]+D_n\,\frac{1}{n}\frac{\partial n}{\partial r}$$

$$\times\frac{\partial nT_i}{\partial r}+Q^e_{\mathrm{NBI}}+Q_{\mathrm{Ohm}}+Q_{ie}(T_e-T_i),\qquad(16)$$

$$\frac{\partial \varepsilon}{\partial t}=\left\{\gamma-\alpha_1\varepsilon-\alpha_2\left[\frac{r}{q}\frac{\partial}{\partial r}\left(\frac{q}{r}\frac{E_r}{B_\phi}\right)\right]^2\right\}\varepsilon+\frac{1}{r}\frac{\partial}{\partial r}\left[rD_\varepsilon\,\frac{\partial \varepsilon}{\partial r}\right],$$
$$(17)$$

with

$$E_r=\frac{1}{|e|}\left[\frac{\partial T_i}{\partial r}+\frac{T_i}{n}\frac{\partial n}{\partial r}\right].\qquad(18)$$

The fluctuation-driven transport dynamics is based on the ion temperature gradient- (ITG-) driven turbulence for the plasma core and resistive pressure-gradient-driven turbulence for the edge. This type of model seems to describe well the transport properties of Tokamak Fusion Test Reactor (TFTR) plasmas.[27] Here we are not attempting to do detailed modeling of discharges, but to describe some of the generic properties. In the Appendix, we give the details of the model used, as well as the form for the power and particle sources. The fluctuation equation only includes the evolution of the (ITG) instabilities, while the edge transport is kept fixed, because we are only interested in the internal transport barriers. In this model, the shear suppression term in the fluctuation equation is based on the Hahm and Burrell[28] extension of the BDT criterion.[20] The shearing rate is given by

$$\omega_s=\frac{\Delta_r}{r\Delta_\theta}\,\frac{r}{q}\,\frac{\partial}{\partial r}\left(\frac{qE_r}{rB_\phi}\right),\qquad(19)$$

where Δ_r and Δ_θ are the radial correlation length and the poloidal correlation angle, respectively. This takes into account the toroidal nature of the plasma and the role of magnetic shear in the suppression. As a result of this change in the form of the shearing term, the α_2 coefficient in Eq. (17) is now

$$\alpha_2=\left(\frac{\Delta_r}{r\Delta_\theta}\right)^2\frac{1}{\gamma}.\qquad(20)$$

The α_1 coefficient has the same form as in Sec. II. Now, however, α_1 has an explicit dependence on T_e, which is time evolved. In the pretransition reversed shear (RS) state, temporal and spatial computational resolution is not a problem because the system evolves on a transport time scale. However, because the transition takes place on a turbulent nonlinear time scale (which can be orders of magnitude faster than the transport time scale), care must be taken. During the transition, time and space resolution issues become much more difficult. Typical q and γ_0 profiles (once again assuming the factorized form for the growth rate) are shown in Fig. 9(a) and the corresponding RS profiles of T_i, T_e, n, and ε are shown in Fig. 9(b). This case is calculated for TFTR parameters of 15 MW neutral beam power, minor radius a of 82 cm, and magnetic field B of 4.7 T. We choose this case because of the simple geometry of TFTR. The circular cross section and the apparently smaller importance of toroidal flow in TFTR because of balanced injection allow us
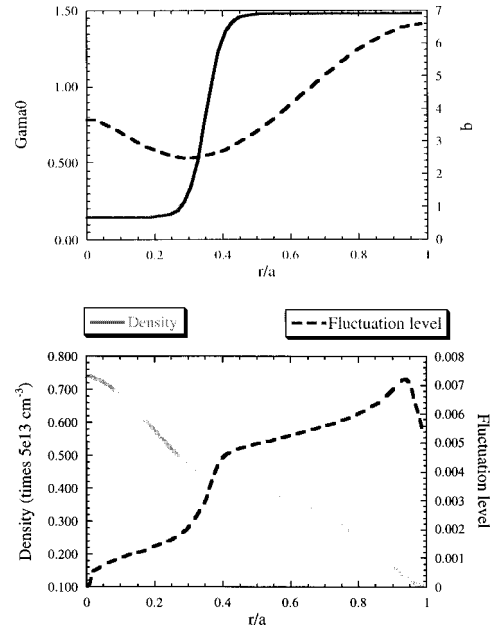

FIG. 9. Radial profiles of γ_0, q [panel (a)], density and fluctuation level [panel (b)] in a ''typical'' reversed magnetic shear case which is below the power threshold for a transition to enhanced confinement.

to ignore the V_ϕ equation, which again simplifies the system. Of course, increased complexity, both with geometry and additional flows, presents more opportunities for triggering and control of the transport barriers, which we will discuss in Sec. V.

For $\alpha_2=0.1$, the transition power threshold is found to be at $\sim24\,\mathrm{MW}\pm2\,\mathrm{MW}$. The α_2 parameter has the largest uncertainties in it as it has both geometric form factors built in, as well as the ratio of the poloidal to toroidal turbulence correlation lengths. Therefore, α_2 probably lies between 0.01 and 0.5 for TFTR. Fortunately there is a weak, $\alpha_2^{-1/3}$, dependence on α_2 in the power threshold (Fig. 10). In this study, we use the total injected power as the control parameter for the transition while typically keeping the nominal width of the deposition profile at $0.2a$. The threshold power is calculated by slowly increasing the power (in increments of 1 MW or less) and allowing the system to relax to steady state before the next incremental increase. The system is determined to have undergone the transition to the ERS regime
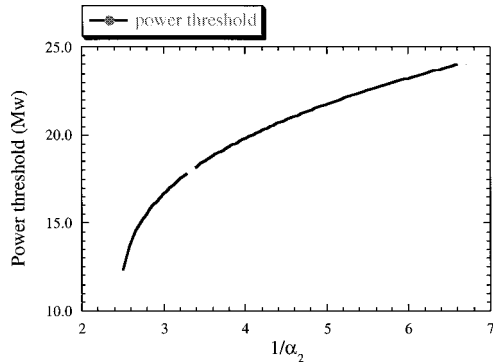

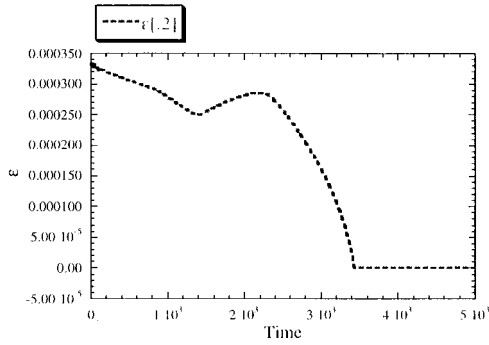FIG. 10. Plot of power threshold in MW versus $1/\alpha_2$.

FIG. 11. A time evolution of the fluctuation level (ε) at r/a equals 0.2, during a transition to enhanced confinement. This shows the rapid change to suppression of the fluctuations. The time unit is 10 μsec.

when a region in the core exhibits fluctuation suppression (Fig. 11) and the confinement time increases.

We can estimate the scaling of the power threshold in terms of dimensionless variables by comparing the general form of the ITG linear growth rate, $\gamma \approx k_\theta \rho_s c_s / L$, with the shearing rate, $\omega_s \approx V_i \rho_i / L^2$. In this analysis, we neglect the intrinsic nonlinear dependence of the profile scale length, L, which we assume constant. The criterion for turbulence suppression gives $\rho_i / L = $ const as the local transition criterion. In this estimate, $k_\theta \rho_s$ is also assumed constant. From this condition, we have the scaling of the local plasma parameters in terms of the magnetic field, $T_i \propto B^2 / m_i$, which, assuming gyroBohm scaling for the pretransition plasmas, gives the scaling of the threshold power

$$\frac{P_{\text{crit}}}{S} \propto \frac{nB^3}{m_i^2}. \tag{21}$$

Here, S is the flux surface area. We have tested this scaling by performing numerical calculations of the power threshold at different magnetic field values, keeping constant the line averaged density. The results are summarized in Fig. 12(a). The numerical results give a scaling exponent for B that is clearly less than 3. By fitting P_{crit}/n by B^λ, we have obtained $\lambda = 2.18 \pm 0.16$. One possible reason for the discrepancy between the numerical scaling and Eq. (21) is that the assumption $T_e \propto T_i$ is not verified. In the magnetic field scan, T_e tends to remain constant while T_i increases with the field. If we use the specific χ_i given in the Appendix, we can calculate the scaling of the threshold with $\tau \equiv T_e / T_i$ also. The local threshold is then $\rho_i / L \propto \tau^{1/2}$. Of course, for $\tau = 1$, we reproduce the previous results. However, if $T_e = $ const, the scaling of the ion temperature at the threshold is $T_i \propto B / \sqrt{m_i}$. This scaling induces the following power threshold scaling:

$$\frac{P_{\text{crit}}}{S} \propto \frac{nB}{m_i}. \tag{22}$$

The scaling exponent of the magnetic field in Eq. (22) is equally as good as the one found in the numerical calculations. This result is also supported by the local scaling of T_i at a radial position close to the beginning of the transition [Fig. 12(b)]. A fit to the numerical results gives T_i
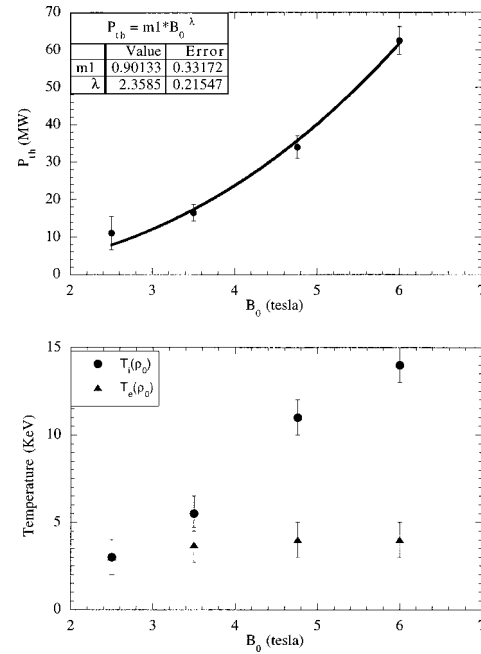

FIG. 12. Panel (a) displays the power threshold dependence on B_0 which is found to be $B_0^{2.3}$. Note that local parameters such as T_i/T_e do not remain constant as shown in panel (b).

$\propto B^{1.3 \pm 0.1}$. This dependence is close to the linear scaling expected for the case where T_e is constant. However, profile changes and, therefore, changes in L may also play a non-negligible role in these scans. This emphasizes that dimensional analysis alone cannot give the full picture and should be treated with some care. In contrast to the threshold power scaling with B, a remarkably robust linear scaling is found with the density (n). This robustness comes from the simple linear scaling of the energy content with n.

Note that because $\rho_i / L \approx $ const for the generic case, the scaling given in Eq. (21) follows from both gyro-Bohm and Bohm transport models. A caveat is necessary—namely that the numerical calculation of the power threshold cannot be done with high accuracy. The reason for the uncertainty in the threshold is that close to the transition a dithering phenomenon exists which is physically based (as will be discussed later) but can obscure when a transition has actually occurred and can, therefore, change the threshold by a small amount. The transition shown in Fig. 11 initiated at the point when the shear parameter from Eq. (19) exceeded the local linear growth rate for the fluctuations. Because ω_s is dependent not only on the shear in the radial electric field, but also on the shear in q, the variation of q around $q_{\min}$ is significant. A small increase in q' can move the transition from outside $q_{\min}$ to inside. Figures 13(a) and 13(b) show the growth rate profiles and the shearing parameter profiles before a transition [Fig. 13(a)] (at lower power) and just as a transition is beginning [Fig. 13(b)]. In this case, the transition clearly initiated inside the $q_{\min}$ surface because the shearing parameter exceeds the growth rate there. However, it should be noted that from r/a of ~ 0.3 to ~ 0.35 the growth rate and shearing parameter profiles are almost equal and tangent. This exact situation leads to the dithering (os-
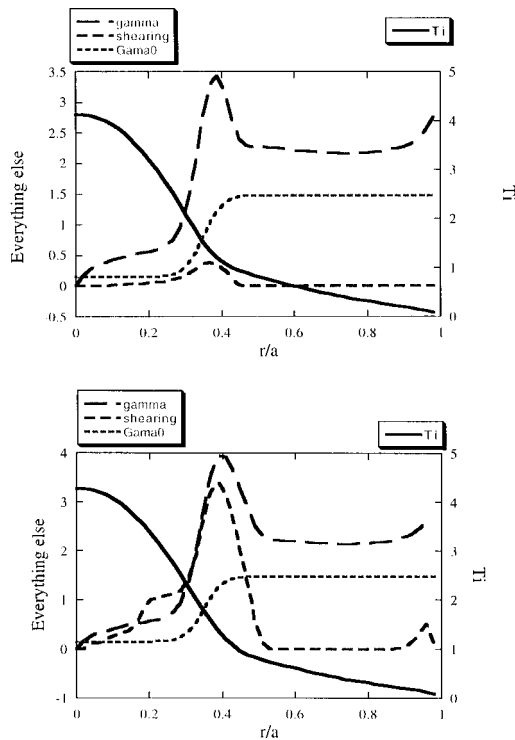
FIG. 13. Profiles of γ, shearing rate, γ_0 and T_i before [panel (a)] and after [panel (b)] the transition power threshold is exceeded. In (a) the shearing rate is smaller than the growth rate everywhere while in (b) the shearing rate exceeds the growth rate in a region from r/a of approximately 0.2 to 0.3. The transition has occurred in this region and is spreading.

FIG. 15. Typical q and E_r profiles are shown in panel (a) while panel (b) displays the shear parameter associated with three deposition profile widths. The same power is deposited in all three cases, but the shear parameter can have widely varying values depending on the deposition width.

cillating) behavior. A small change in the profiles can locally push one larger than the other, which in turn modifies the profile and reverses the situation. This change then can cause oscillations in the computations (see Fig. 14) whenever the two profiles are approximately equal in magnitude and locally tangent. Indeed, oscillations around the radial location where the profiles become marginal (i.e., where the fluctuations are just suppressed), possibly of this type, have been reported on TFTR at the edge of the transition region by Mazzucato.[29] In most of the configurations we have investigated, even after the transition has fully evolved, the profiles at the edge of the ERS region tend to have this characteristic, allowing or causing this type of oscillation to occur. This near-criticality (to suppression) type of relaxation oscillation
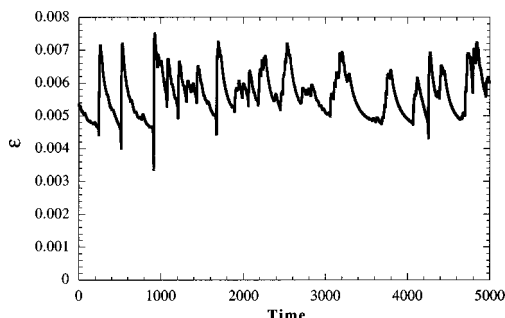
FIG. 14. Local oscillations in the fluctuation level shown in a case in which the transition has occurred. These oscillations are seen just outside the transitioned region at $r/a \sim 0.38$ where the shearing rate and the growth rate are nearly tangent to each other [see Fig. 13(b) for example].
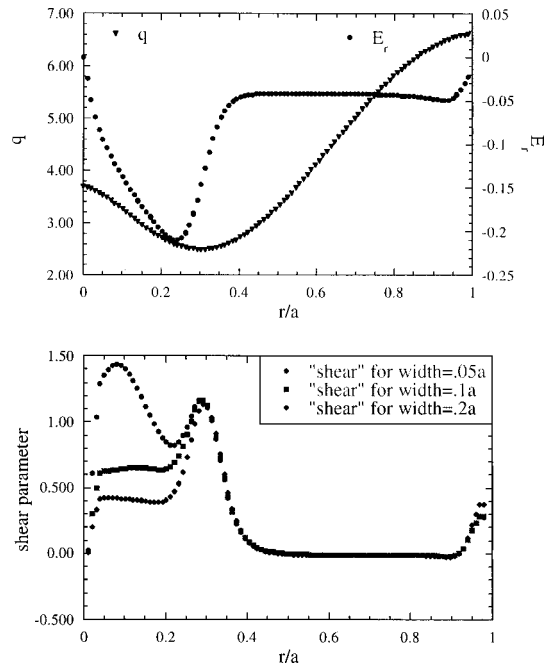
suggests some possible control mechanisms, to prevent impurity accumulation, which are investigated and discussed in the next section.

The key ingredients for a transition to ERS are low local instability growth rate and steep temperature and or density gradients (usually requiring peaked deposition profiles) leading to a steep pressure profile. These elements can be aided by a favorable q gradient. All of these factors are caused or amplified by the reverse shear region which gives the low growth rate (this can also be helped by the reduction in growth rate because of the Shafranov shift[14] mentioned earlier, but not included in this model) and produces the steep gradient because of the localization of the power deposition inside the transition point. For a given power, the more localized the deposition is inside the q_{min} region, the lower the power threshold becomes because more flux comes through the q_{min} surface, giving a steeper gradient for a given diffusivity. Narrowing the deposition profile cannot only decrease the power threshold by increasing the flux through the q_{min} surface but can also move the initiation point for the transition by steepening the gradient in E_r well inside the q_{min} surface. Figure 15(a) shows a typical q profile and a typical pretransition E_r profile in which the alignment of the q_{min} position and the outer gradient in E_r (outside the minimum in E_r) is apparent. Figure 15(b) shows the shearing parameter for three deposition widths, 0.2, 0.1, and 0.05a. An inner peak in the shearing parameter grows as the deposition profile narrows. This peak is located on the inner (inside the E_r minimum) gradient of E_r and can cause the transition to start well inside q_{min}. The power threshold difference observed in TFTR when using tritium (T) beams versus deuterium (D) beams[24] (a lower threshold is seen for deuterium)

Phys. Plasmas, Vol. 5, No. 4, April 1998
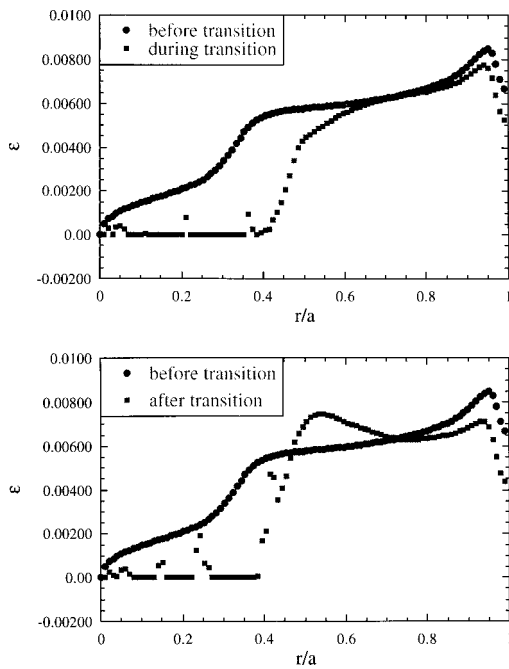
Newman *et al.* 947

FIG. 16. Radial profiles of the fluctuation levels before and during a transition [panel (a)] show the transient decrease in the fluctuation level outside the transition region due to a transiently decreased flux. The profiles before and after [panel (b)] the transition indicate an increased fluctuation level just outside the transition region due to an increased gradient and therefore linear drive.

FIG. 17. Radial profiles of ion temperature (T_i) and density (N) before and after a transition.

could be explained via the deposition profiles for the two cases. If the D beams deposit more power/particles inside the q_{min} surface than the T beams, the threshold would be proportionally lower.

Even though the fluctuations are relatively low in the RS region before the transition, the anomalous transport is still much larger than neoclassical. Therefore, when the transition occurs, the core region (the region inside the transport barrier) becomes a very efficient power and particle accumulator. An interesting point to note is that after the transition but before reaching a new steady state, a transient decrease occurs in the fluxes out of the core. This decrease occurs because the diffusivities drop rapidly (at the transition) while the profiles build up more slowly, so the flux (for example $\Gamma_n = D_n/\nabla n$) must decrease until the new steady-state profile builds up. This is just a straightforward consequence of the inequality $\tau = (\Delta x_b)^2/D < \tau_{deposition}$, namely that the barrier is thin, so local transport times exceed the heating rate. Here, Δx_b is the barrier width. The decreased flux can lead to a transient decrease in the fluctuation level [Fig. 16(a)] outside the barrier as the large anomalous diffusion there relaxes the gradients outside the barrier. This is similar to the scrape-off-layer (SOL) plasma behavior during H mode in which SOL fluctuations (nominally outside the barrier) drop after the transition. When the system reaches its new equilibrium, the flux again increases (to balance the input), and the fluctuation levels return to their earlier levels. When steady state is reached, the fluctuation levels just beyond the barrier footprint are often higher [Fig. 16(b)] than before the transition because of increased local growth rates from the locally steepened gradient. The efficient accumulation of particles
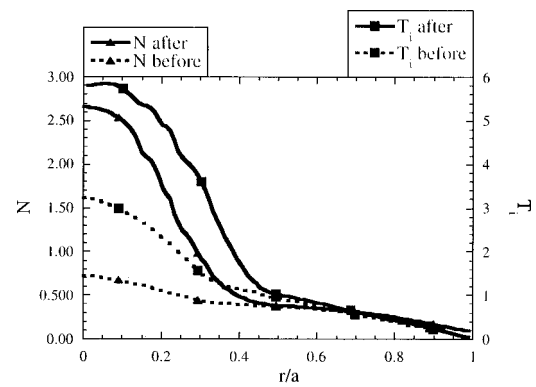
and heat can clearly lead to very large increases in the temperatures and densities if the system is allowed to evolve to a steady state without any other large scale transport event (i.e., a disruption of some type). The profiles of density and temperature are shown in Fig. 17 before and after the transition in or near steady state. The power in this case was approximately 5 MW above the power threshold. One can easily see that the transition has propagated well outside the reversed shear region. In fact, in this case the steep pressure gradients that exist outside the RS region are unstable to ideal ballooning modes using the Pogutse–Yurchenko criteria.[30]

The propagation of the transition in this model has two distinct regimes. In both of these temporal regions the transition is moderated by the spreading of the radial electric field shear. First, a very rapid transition occurs in the core region in which the RS (and other effects) has provided a lowered growth rate. In this region, the transition propagates on a nonlinear time scale [Fig. 18(a)] and resembles the supercritical transitions exhibited by some VH-mode models[18] and by the simpler model from the previous section. The entire transition for the "supercritical" region (approximately $0.3a$) has occurred in less than $5\tau_g$, where $\tau_g \approx \gamma^{-1}$ is the fluctuation growth time. As the transition moves out into the "subcritical" region where the instability growth rate is larger, the propagation slows down [Fig. 18(b)] to a hybrid propagation velocity dominated by the neoclassical (that is posttransition) diffusion time because of the Maxwell criteria. In this regime the transition has taken more then $500\tau_g$ to cover less than an additional $0.2a$. These time scales are in qualitative agreement with the propagation velocities analytically predicted by Lebedev and Diamond.[23]

This more complete model, as in the simpler model, shows a strong hysteresis effect (Fig. 19), allowing the power to be lowered by a significant amount after the transition is obtained while still maintaining the ERS regime. In addition to the asymmetry in the forward and backward threshold powers (the hysteresis), an asymmetry exists in the time scales involved in the forward and backward transitions similar to that seen in experiment.[31] The forward transition occurs more rapidly (for a given increment above critical) than the back transition does (Fig. 20). This difference can be understood to follow from a number of causes. First,
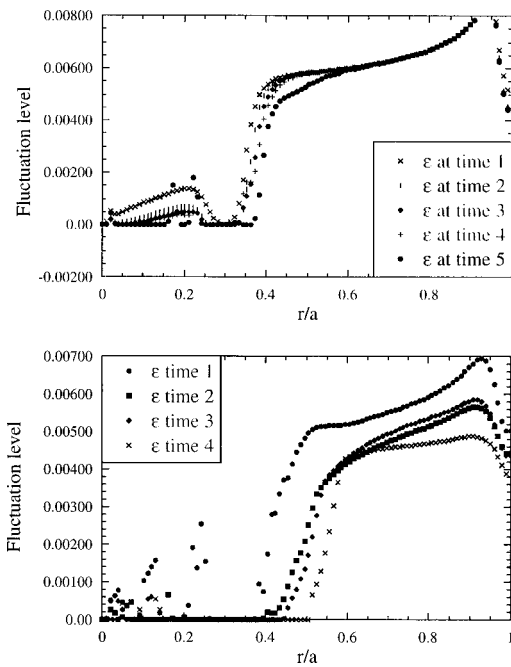
FIG. 18. Profiles of the fluctuation level at different times during a transition. The early part of the transition [panel (a)] occurs rapidly with the time spacing of the profiles of 0.0001 sec. The later part of the transition [panel (b)] occurs much more slowly with the time spacing here between profiles of 0.02 sec.

FIG. 20. Time evolutions of the fluctuations at r/a of 0.25 during a forward transition is displayed in panel (a) and for a back transition in panel (b). The forward transition is seen to be at least 20 times faster than the back transition.

asymmetry exists in the source of the flux which maintains the gradient. In the forward transition, the transition bootstraps itself up, which is a positive feedback on the transition. In the back transition, however, the increased diffusivity increases the flux, which tends to inhibit the relaxation of the gradient and, therefore, slows the back transition via negative feedback. Additionally, the increased gradients that exist before the back transition can cause a reduction in the local growth rate induced by the Shafranov shift, which will decrease the anomalous diffusion even after the back transition, again acting as a negative feedback, which slows its propagation.

V. SCHEMES FOR CONTROLLING INTERNAL TRANSPORT BARRIERS

Two types of control systems are necessary for setting up operational scenarios with transport barriers: (1) setting up and maintaining the barrier in the most expeditious way,
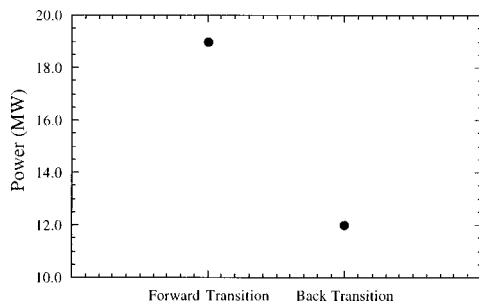

FIG. 19. The power threshold for the forward transition is 19 MW while the back transition threshold is 12 MW.
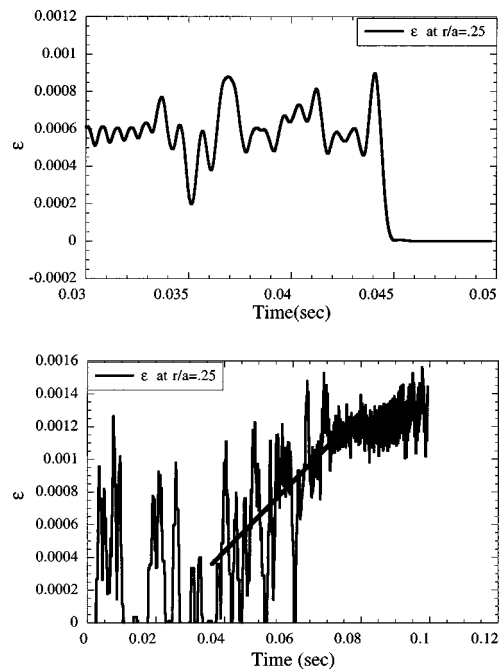
and (2) lowering the barrier to avoid impurity and ash accumulation at the plasmas core. Table I list the profile parameters that need to be controlled together with some obvious techniques to achieve this control. In this section, we will discuss some of these techniques and the results obtained by modeling several of the proposed approaches.

In Sec. IV we noted that the apparent power threshold is reduced by transient pulses (or oscillations). This type of trigger is reminiscent of L–H transitions triggered by the heat pulse associated with sawtooth oscillations. In and of itself this may have relevance to the different types of transitions observed on TFTR. However, it also suggests possible mechanisms for triggering the transitions at powers which are significantly below the "steady state threshold." The mechanism for such a subcritical trigger is quite straightforward. A transient pulse in the pressure (from any source) will propagate outward. Such a pulse causes a local transient steepening of the pressure gradient and, because it is local, an increase in the radial electric field shear. This transient increase in E_r' then can locally quench the fluctuations, reducing the diffusivity and causing the positive feedback (growth in gradients, etc.) which underlies the entire model. Effectively, it is the concept of a transient local transition coupled to positive feedback and hysteresis that allow these subcritical transitions to occur and propagate radially. Within a toroidal magnetic confinement device, a wide range of internal and external triggers are possible. Probably the most common of these triggering mechanisms, and the one which can explain the intrinsic variations in observed thresholds, is a simple transport event. Contrary to diffusive transport modeling, turbulent transport is not a smooth continuous process. It is instead a bursty, spiky process, possibly better

Phys. Plasmas, Vol. 5, No. 4, April 1998

Newman *et al.*   949

represented by a model that incorporates noise-induced fluctuations as the transport dynamics of a self-organized critical system[32–34] than the more typical mean field diffusion model. Within the context of such a model based on gradient-driven turbulent transport and backed up by experimental observation,[35] the various fluxes are found to be quite bursty. These bursts in flux will necessarily give rise to concomitant fluctuations in the gradients. Because these flux bursts have a distribution in sizes, large ''transport events'' are possible. One of these flux spikes can cause the gradient to locally and instantaneously become super-critical and produce local transitions with positive feedback allowing the growth and propagation of the barrier. In general, the dynamics of such self-organized critical gradient transport constrain the local gradient do not deviate very far or very frequently from the system's preferred slope. This makes it unlikely that these intrinsic fluctuations would trigger transitions that were more than slightly (more than a few MW in our cases) subcritical. Using the idea of a transport-event-driven trigger, it is not difficult to imagine cases in which the transition can be strongly subcritical. One such situation is that of a magnetohydrodynamic (MHD) instability confined to the core (i.e., sawtooth oscillations). A fast MHD instability could rapidly flatten the profile inside the inversion radius (r_{inv}), which we will take to be inside r_{min}. This will send a large transient pulse of flux out through the q_{min} surface, causing a large local jump in the gradient and triggering a local transition to ERS confinement. This type of event could account for the difference between the Type I and Type II ERS transitions observed on TFTR. All that is required is that the power be above the back transition threshold, which is typically much lower than the regular transition threshold (from the ratio of the pre/posttransition diffusivities as discussed earlier) and $r_{inv} \ll r_{min}$. This type of scenario is more likely to occur with a weak central magnetic shear than a strongly negative central magnetic shear configuration because of the stabilizing effect of the negative magnetic shear on magnetohydrodynamic (MHD) instabilities. To properly investigate such a scenario one must include MHD stability and transport in the bifurcation model. This inclusion is beyond the scope of the present investigation. It does lead to the intriguing possibility that one could trigger a confined MHD event in order to trigger the ERS transition.

The next possible methods for active triggering follow the line of actively and transiently reducing the local threshold. Two methods for doing this are through active profile control of the V_θ and V_ϕ flows. Since the addition of V_ϕ' or V_θ' (with the correct sign) increases E_r', it reduces the amount of E_r' that must come from the pressure gradient. This in turn reduces the power threshold for the transition. While V_θ is likely damped in the core, a narrow region of sheared poloidal flow may be driven by IBW[2,26] as on PBX-M. It is perhaps even easier to modify V_ϕ' because this can be done by tailoring the beam deposition profiles and/or by balancing beams and does not require any additional external power. V_ϕ' has been added to the present model and indeed can reduce or increase the power threshold as was shown in Sec. III. However, to do this properly, the beam deposition profiles must evolve with the background profiles
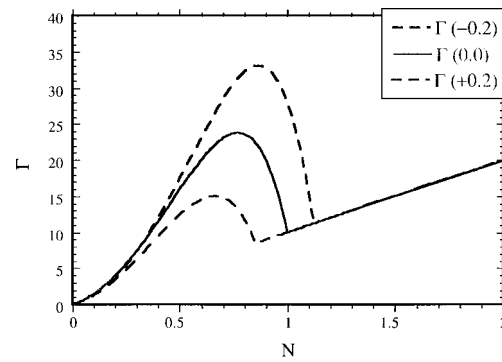

FIG. 21. Bifurcation curves with the addition of a sheared toroidal flow exhibit a large effect on the forward transition threshold (the top peak) but a smaller effect on the back transition threshold (the valley).

which are not contained in the present models. If the sign of the V_ϕ' (or V_θ') term is opposite to that of the ∇P_i term, then the threshold can actually be increased. The change in the transition power can most clearly be seen in the hysteresis curves modified by V_ϕ' (Fig. 21). The forward transition power threshold changes by more than 20% in this illustration; however, because the back transition is moderated by the neoclassical diffusion, the changes in the back transition level are much smaller. This technique can lead to scenarios in which one can trigger the transition and a back transition to control the profiles and accumulation rates and suggests that operating above but close to the back transition power threshold is the most favorable regime for the various control and triggering schemes.

A final mechanism for triggering the transition is by using a combination of rf heating and pellets. If a region just inside the q_{min} surface is heated (thus, steepening the local profile), allowed to come to equilibrium, and then a pellet is fired into the core, the transient-added particle flux from the pellet comes through the heated region and a transient increase occurs in the pressure gradient. This in turn can trigger a confinement transition (Fig. 22). This type of trigger may be of particular interest on devices such as Tore Supra
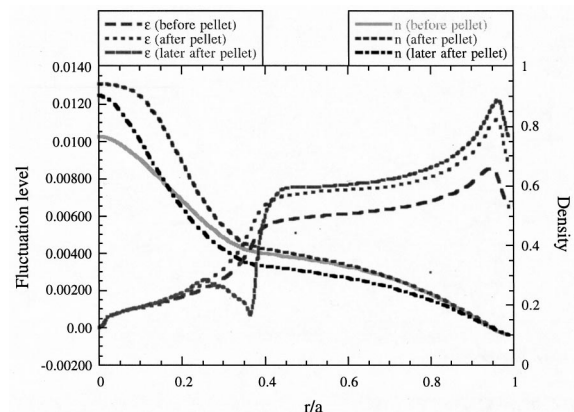

FIG. 22. Profiles of the fluctuation level and the density before, immediately after, and some time after a pellet is deposited in the core. These profiles display the evolution to a transition caused by the transient pulse in the flux from the pellet.
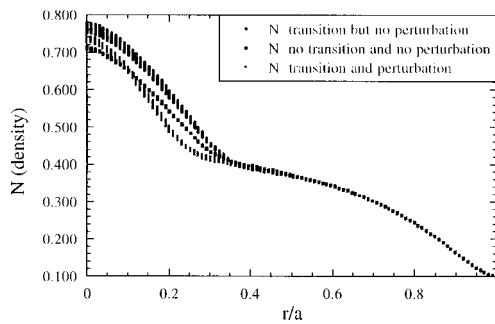
FIG. 23. Density profiles with and without a transition and with and without perturbations to the q_{min} position demonstrate the possibility of controlling the final profiles with small perturbations.

FIG. 24. The effect of the perturbations is seen in the time evolutions of both the fluctuation level (ε) and the density (n) at r/a of 0.25.

on which the current profile can be controlled via Lower Hybrid current drive[36] which can also serve as an off-axis heating source.

As mentioned earlier, for the ERS confinement mode to be useful, it must not only be triggered at reasonable powers, but the accumulation rates must be controlled. Certainly using the hysteresis effect to lower the power input after the transition can help. Even then, one would like to be able to selectively open a valve in the barrier. One possible method to do this is via initiating transport events by causing a local back transition using some local V'_ϕ or V'_θ drive to force the system to locally back transition. This will not cause the entire system to back transition but will cause a transport event to propagate out, thereby transiently removing some of the confinement.

A mechanism which may offer more control is q-profile modification via current drive. If the q_{min} surface can be moved in and out a small amount, as a function of time (via local off-axis current drive), a large increase in the flux can be induced. This is caused by the radial ''wiggling'' of the barrier through a wiggling of the growth rate profiles that are tied to the reversed shear region. By controlling the amplitude and frequency of the perturbations of the q profile, the background profiles (accumulation rates) can be controlled (Fig. 23). In this case, the power is 1 MW above the forward transition threshold. Without any perturbation, the central density can be seen to effectively run away after the transition. However, with a 20% perturbation in the q_{min} position, the central density can be stabilized at a value only 10% higher than the untransitioned case. Near the barrier footpoint, oscillations can be seen in ε, T_e, T_i, and n which coincide with the movement of the q profile (Fig. 24). Varying the frequency and amplitude of the perturbations can control the final, steady-state profiles. The frequency of the q_{min} motion should be between the nonlinear transition time and the neoclassical diffusion time to allow time for the transitions to occur but not enough time for the profiles to be fully slaved to the oscillations. The current drive requirements for such control are relatively modest. A simple estimate of the percentage of the current displaced by shifting δq from its minimum position by Δr is $\Delta I/I \approx (\Delta r r_{min}/a^2) \times (q_a \delta q/q_{min})$. For the case we have considered, this estimate gives $\Delta I/I \approx 0.02$.
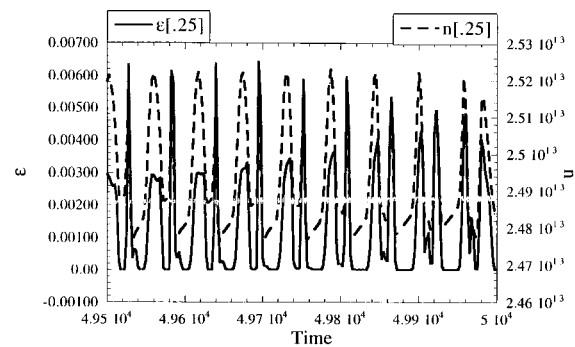
VI. CONCLUSION

During our study of the dynamics and control of core transport barriers in discharges with reversed magnetic shear we found the following principal results:

(1) The basic qualitative (and some quantitative) features of the transition evolution are captured by a simple two-field model for the density gradient and fluctuation intensity which incorporates E'_r-drive transport bifurcation dynamics as well as reduction of pretransition instability growth rate by magnetic shear reduction or reversal.

(2) The basic conclusions of the simple model are supported by more detailed investigations which incorporate toroidal momentum and ion and electron heat transport. In particular, the transition may be influenced by the sign of V_ϕ relative to ∇P_i. In the context of the more complete model, the Type I transitions recently observed in TFTR ERS discharges may be explained by a MHD event triggering the transition. Also, this model exhibits oscillatory bursts close to the transition threshold in agreement with recent TFTR observations.

(3) Dimensional analysis indicates that (assuming gyro-Bohm transport and constant T_i/T_e) the threshold power for diamagnetic E'_r-transport bifurcation scales as $P_{crit}/S \propto nB^3/m_i^2$, with $\rho^* \approx$ const across the transition. Self-consistent profile evolution (which introduces nonlinear dependence of profile scale lengths) suggests that this prediction be modified to $P_{crit} \propto nB^\alpha$ where $\alpha = 2.2 \pm 0.2$. The change in the exponent is mostly because of the weak change of the electron temperature with the magnetic field.

(4) A number of transition and profile control techniques are suggested by these studies. These include transient heating (which exploits hysteresis), rf flow drive, and pellet injection as ways of lowering the transition threshold or controlling it. The q-profile modulation is shown as a possible alternative technique to control the barrier and avoid the accumulation of impurities.

Many questions pertinent to the enhanced reversed shear confinement still remain unanswered, including:

(1) The role of poloidal rotation in triggering the transition and maintaining the barrier. In particular, the strong electric field characteristics of such plasmas may result

in breakdown of the magnetic viscosity, thus vitiating the conventional wisdom that poloidal rotation in the core plasma is heavily damped.

(2) The response of the electron transport and the dynamics of electron transport barrier formation. The electron channel appears to behave qualitatively differently from the ion particle and momentum transport channels in several experiments.

These issues will be addressed in a future publication.

APPENDIX

The transport model used in Sec. IV for the determination of the power threshold is based on two turbulence mechanisms: (1) ion temperature gradient- (ITG-) driven instabilities at the plasma core and (2) resistive ballooning turbulence at the plasma edge. These transport dynamics seem to describe well Tokamak Fusion Test Reactor (TFTR) plasmas.[27] Here we use a simplified form of the transport models used in Ref. 37 for the ITG instability. We have taken the toroidal η_i branch as described in Ref. 38. The explicit form of the linear growth rate is

$$\gamma_{\eta_i} = k_\theta \rho_s \frac{c_s}{a} f(\hat{S}) \left(\frac{a}{R}\right)^{1/2} \left(\frac{a}{L_n} + \frac{a}{L_T}\right)^{1/2} \left(\frac{T_i}{T_e}\right)^{1/2}, \quad (A1)$$

where $L_n = n \, (dn/dr)^{-1}$ and $L_T = T_i \, (dT_i/dr)^{-1}$ are the characteristic scale lengths of the density and ion temperature, respectively. The magnetic shear, $\hat{S}$, stabilization effect is manifest through the form factor $f(\hat{S})$. The diffusivities expressed in terms of the fluctuation amplitude (ε) are

$$\chi_{i\,\eta_i} = k_\theta \rho_s c_s a \left(\frac{a}{R}\right)^{1/2} \left(\frac{a}{L_n} + \frac{a}{L_T}\right)^{-1/2} \left(\frac{T_i}{T_e}\right)^{1/2} \varepsilon^2, \quad (A2)$$

$$\chi_{e\,\eta_i} = D_{\eta_i} = k_\theta \rho_s \frac{c_s}{a\nu_e} \left(\frac{a^2}{L_n R}\right)^{1/2} \left(1 + \frac{L_n}{L_T}\right)^{1/2} \left(\frac{T_i}{T_e}\right)^{1/2} \chi_{i\,\eta_i}. \quad (A3)$$

The explicit form of the linear growth rate, Eq. (A1), goes into the fluctuation evolution equation, Eq. (17) (see Sect. IV). The fluctuation amplitude resulting from solving this equation is used in calculating the η_i contribution to the diffusivities in Eqs. (A2) and (A3). The form of the resistive ballooning diffusivity adopted in this calculation is the one given in Ref. 39:

$$D_{RB} = 2\sqrt{2} \pi^2 q^2 \rho_s c_s \frac{R}{a} \frac{\nu_e}{\Omega_e} \left(\frac{a}{L_n} + \frac{a}{L_T}\right). \quad (A4)$$

Here, ν_e is the electron collisionality and Ω_e is the electron cyclotron frequency. We had to use a multiplier of the order

of 20 to reproduce the TFTR results from Ref. 37. This term only affects the plasma edge and is not dynamically evolved with the fluctuation equation. Therefore, the diffusivities in Eqs. (14)–(16) (see Sect. IV) are

$$D_n = D_{\text{neo}} + D_{RB} + D_{\eta_i}, \quad (A5)$$

$$\chi_i = \chi_{\text{ineo}} + \chi_{i\,\eta_i} + D_{RB}, \quad (A6)$$

$$\chi_e = \chi_{\text{eneo}} + \chi_{e\,\eta_i} + D_{RB}. \quad (A7)$$

In all three diffusivities, the contribution from neoclassical transport has been included. The diffusivity in the fluctuation equation is taken to be a constant.

In this model, the source terms are assumed to have a very simple form. The neutral beam is assumed to be monoenergetic and its radial deposition profile is a Gaussian profile with a width W_{NBI}. An edge source term, S_{gp}, is included in the density equation, Eq. (14) (see Sect. IV), as a way to control the density. The form of the ohmic heating term in Eq. (16) (see Sect. IV) is consistent with the assumed q profile, and the energy transfer term between electrons and ions has the standard form

$$Q_{ie} = -Q_{ei} = 3 \frac{m_e}{m_i} n \nu_e, \quad (A8)$$

where m_e and m_i are the electron and ion mass, respectively.

[1]Y. Koide, M. Kikuchi, M. Mori, S. Tsuji, S. Ishida, N. Asakura, Y. Kamada, T. Nishitani, Y. Kawano, T. Hatae, T. Fujita, T. Fukuda, A. Sakasai, T. Kondoh, R. Yoshino, and Y. Neyatani, Phys. Rev. Lett. **72**, 3662 (1994).

[2]B. LeBlanc, S. Batha, R. Bell, S. Bernabei, L. Blush, E. de la Luna, R. Doerner, J. Dunlap, A. England, I. Garcia, D. Ignat, R. Isler, S. Jones, R. Kaita, S. Kaye, H. Kugel, F. Levinton, S. Luckhardt, T. Mutoh, M. Okabayashi, M. Ono, F. Paoletti, S. Paul, G. Petravich, A. Post-Zwicker, N. Sauthoff, L. Schmitz, S. Sesnic, H. Takahashi, M. Talvard, W. Tighe, G. Tynan, S. von Goeler, P. Woskov, and A. Zolfaghari, Phys. Plasmas **2**, 741 (1995).

[3]M. Greenwald, D. Gwinn, S. Milora, J. Parker, R. Parker, S. Wolfe, M. Besen, F. Camacho, S. Fairfax, C. Fiore, M. Foord, R. Gandy, C. Gomez, R. Granetz, B. LaBombard, B. Lipschultz, B. Lloyd, E. Marmar, S. McCool, D. Pappas, R. Petrasso, R. Pribyl, J. Rice, D. Schuresko, Y. Takase, J. Terry, and R. Watterson, Phys. Rev. Lett. **53**, 352 (1984).

[4]F. Wagner, G. Becker, K. Behringer, D. Campbell, A. Eberhagen, W. Engelhardt, G. Fussmann, O. Gehre, J. Gernhardt, G. V. Gierke, G. Haas, M. Huang, F. Karger, M. Keilhacker, O. Klüber, M. Kornherr, K. Lackner, G. Lisitano, G. G. Lister, H. M. Mayer, D. Meisel, E. R. Müller, H. Murmann, H. Niedermeyer, W. Poschenrieder, H. Rapp, H. Röhr, F. Schneider, G. Siller, E. Speth, A. Stäbler, K. H. Steuer, G. Venus, O. Vollmer, and Z. Yü, Phys. Rev. Lett. **49**, 1408 (1982).

[5]F. M. Levinton, M. C. Zarnstorff, S. H. Batha, M. Bell, R. E. Bell, R. V. Bundy, C. Bush, Z. Chang, E. Fredrickson, A. Janos, J. Manickam, A. Ramsey, S. A. Sabbagh, G. L. Schmidt, E. J. Synakowski, and G. Taylor, Phys. Rev. Lett. **75**, 4417 (1995).

[6]E. J. Strait, L. L. Lao, M. E. Mauel, B. W. Rice, T. S. Taylor, K. H. Burrell, M. S. Chu, E. A. Lazarus, T. H. Osborne, S. J. Thompson, and A. D. Turnbull, Phys. Rev. Lett. **75**, 4421 (1995).

[7]E. A. Lazarus, G. A. Navratil, C. M. Greenfield, E. J. Strait, M. E. Austin, K. H. Burrell, T. A. Casper, D. R. Baker, J. C. DeBoo, E. J. Doyle, R. Durst, J. R. Ferron, C. B. Forest, P. Gohil, R. J. Groebner, W. W. Heidbrink, R.-M. Hong, W. A. Houlberg, A. W. Howald, C.-L. Hsieh, A. W. Hyatt, G. L. Jackson, J. Kim, L. L. Lao, C. J. Lasnier, A. W. Leonard, J. Lohr, R. J. La Haye, R. Maingi, R. L. Miller, M. Murakami, T. H. Osborne, L. J. Perkins, C. C. Petty, C. L. Rettig, T. L. Rhodes, B. W. Rice, S. A. Sabbagh, D. P. Schissel, J. T. Scoville, R. T. Snider, G. M. Staebler, B. W. Stallard, R. D. Stambaugh, H. E. St. John, R. E. Stockdale, P. L.

Taylor, D. M. Thomas, A. D. Turnbull, M. R. Wade, R. Wood, and D. Whyte, Phys. Rev. Lett. **77**, 2714 (1996).

[8] Y. Koide and JT-60 Team, Phys. Plasmas **4**, 1623 (1997).

[9] V. B. Lebedev, P. H. Diamond, M. B. Isichenko, P. N. Yushmanov, D. E. Newman, B. A. Carreras, V. E. Lynch, T. S. Hahm, W. M. Tang, G. Rewoldt, K. Avinash, A. Smolyakov, IAEA-CN-64/D1-3, *Proceedings of Sixteenth International Atomic Energy Agency Fusion Energy Conference*, Montreal, Canada, October 7–11, 1996 (International Atomic Energy Agency, Vienna, 1997).

[10] P. H. Diamond, V. B. Lebedev, D. E. Newman, B. A. Carreras, T. S. Hahm, W. M. Tang, G. Rewoldt, and K. Avinash, Phys. Rev. Lett. **78**, 1472 (1997).

[11] B. B. Kadomtsev and O. P. Pogutse, Sov. Phys. JETP **24**, 1172 (1967).

[12] C. Kessel, J. Manickam, G. Rewoldt, and W. M. Tang, Phys. Rev. Lett. **72**, 1212 (1995).

[13] J. Y. Kim and M. Wakatani, Phys. Plasmas **2**, 1012 (1995).

[14] M. A. Beer, G. W. Hammett, G. Rewoldt, E. J. Synakowski, M. C. Zarnstorff, and W. Dorland, Phys. Plasmas **4**, 1792 (1997).

[15] G. Rewoldt, L. L. Lao, and W. M. Tang, Phys. Plasmas **4**, 3293 (1997).

[16] P. H. Diamond, Y-M. Liang, B. A. Carreras, and P. W. Terry, Phys. Rev. Lett. **72**, 2565 (1994).

[17] B. A. Carreras, D. Newman, P. H. Diamond, and Y.-M. Liang, Phys. Plasmas **1**, 4014 (1994).

[18] P. H. Diamond, V. B. Lebedev, D. E. Newman, and B. A. Carreras, Phys. Plasmas **2**, 3685 (1995).

[19] F. L. Hinton and G. M. Stabler, Phys. Fluids B **5**, 1281 (1993).

[20] H. Biglari, P. H. Diamond, and P. W. Terry, Phys. Fluids B **2**, 1 (1990).

[21] R. E. Bell, F. M. Levinton, S. H. Batha, E. J. Synakowski, and M. C. Zarnstorff, ''Core poloidal rotation and internal transport barrier formation in TFTR,'' to be published in Plasma Phys. Controlled Fusion.

[22] G. L. Jackson, J. Winter, T. S. Taylor, K. H. Burrell, J. C. DeBoo, C. M. Greenfield, R. J. Groebner, T. Hodapp, K. Holtrop, E. A. Lazarus, L. L. Lao, S. I. Lippmann, T. H. Osborne, T. W. Petrie, J. Phillips, R. James, D. P. Schissel, E. J. Strait, A. D. Turnbull, W. P. West, and DIII-D Team, Phys. Rev. Lett. **67**, 3098 (1991).

[23] V. B. Lebedev and P. H. Diamond, Phys. Plasmas **4**, 1087 (1997).

[24] E. J. Synakowski, S. H. Batha, M. A. Beer, M. G. Bell, R. E. Bell, R. V. Budny, C. E. Bush, P. C. Efthimion, G. W. Hammett, T. S. Hahm, B. LeBlanc, F. Levinton, E. Mazzucato, H. Park, A. T. Ramsey, G. Rewoldt, S. D. Scott, G. Schmidt, W. M. Tang, G. Taylor, and M. C. Zarnstorff, Phys. Rev. Lett. **78**, 2972 (1997).

[25] G. G. Craddock and P. H. Diamond, Phys. Rev. Lett. **67**, 1535 (1991).

[26] M. Ono, Phys. Fluids B **5**, 241 (1993).

[27] G. Bateman, Phys. Fluids B **4**, 634 (1992).

[28] T. S. Hahm and K. H. Burrell, Phys. Plasmas **2**, 1648 (1995).

[29] E. Mazzucato, S. H. Batha, M. Beer, M. Bell, R. E. Bell, R. V. Budny, C. Bush, T. S. Hahm, G. W. Hammett, F. M. Levinton, R. Nazikian, H. Park, G. Rewoldt, G. L. Schmidt, E. J. Synakowski, W. M. Tang, G. Taylor, and M. C. Zarnstorff, Phys. Rev. Lett. **77**, 3145 (1996).

[30] O. P. Pogutse and E. I. Yurchenko, Fiz. Plazmy **5**, 786 (1979).

[31] E. J. Synakowski, S. H. Batha, M. A. Beer, M. G. Bell, R. E. Bell, R. V. Budny, C. E. Bush, P. C. Efthimion, R. J. Fonck, T. S. Hahm, G. W. Hammett, J. Kim, B. LeBlanc, F. Levinton, E. Mazzucato, H. Park, A. T. Ramsey, G. Schmidt, G. Rewoldt, S. D. Scott, G. Taylor, M. C. Zarnstorff, *Proceedings of 24th European Physical Society Conference on Controlled Fusion and Plasma Physics*, Berchtesgaden, Germany, June 9–13, 1997, edited by M. Schittenhelm, R. Bartiromo, and F. Wagner (European Physical Society, Petit-Lancy, 1997) pg. 323.

[32] P. Bak, C. Tang, and K. Weisenfeld, Phys. Rev. Lett. **59**, 381 (1987).

[33] D. E. Newman, B. A. Carreras, P. H. Diamond, and T. S. Hahm, Phys. Plasmas **3**, 1858 (1996).

[34] B. A. Carreras, D. Newman, V. E. Lynch, and P. H. Diamond, Phys. Plasmas **3**, 2903 (1996).

[35] B. A. Carreras, C. Hidalgo, E. Sanchez, M. A. Pedrosa, R. Balbin, I. Garcia-Cortes, B. V. Milligen, D. E. Newman, and V. E. Lynch, Phys. Plasmas **3**, 2664 (1996).

[36] X. Litaudon, R. Arslanbekov, G. T. Hoang, E. Joffrin, F. Kazarian-Vibert, D. Moreau, Y. Peysson, P. Bibet, P. Froissard, M. Goniche, G. Rey, J. Ferron, and K. Kupfer, ''Stationary magnetic shear reversal during lower hybrid experiment in Tore Supra,'' to be published in Plasma Physics and Contolled Fusion.

[37] J. E. Kinsey, G. Bateman, A. Kritz, and A. Redd, Phys. Plasmas **3**, 561 (1996).

[38] H. Biglari, P. H. Diamond, and M. N. Rosenbluth, Phys. Fluids B **1**, 109 (1989).

[39] P. N. Guzdar, J. F. Drake, D. McCarthy, A. B. Hassam, and C. S. Liu, Phys. Fluids B **5**, 3712 (1993).